Rare Metal Materials and Engineering
Volume 50, Issue 3, March 2021
Available online at www.rmme.ac.cn

Science Press

Cite this article as: Rare Metal Materials and Engineering, 2021, 50(3): 0807-0815.

ARTICLE

Mechanical Properties of Bimodal AZ91 Alloy Prepared by Low-Temperature Slow Rate Extrusion and Electrical Pulse Treatment

Wu Hongfei[1], Fan Jianfeng[1,2], Shan Zhaohui[1], Zhang Hua[1,2], Zhang Qiang[1,2], Deng Kunkun[1,2], Wu Yucheng[1], Li Weiguo[1], Dong Hongbiao[3], Xu Bingshe[1]

[1] Key Laboratory of Interface Science and Engineering in Advanced Materials, Ministry of Education, Taiyuan University of Technology, Taiyuan 030024, China; [2] Shanxi Key Laboratory of Advanced Magnesium-based Materials, Taiyuan 030024, China; [3] Department of Engineering, University of Leicester, Leicester LE1 7RH, UK

Abstract: Low-temperature slow rate extrusion (LTSRE) and electrical pulse treatment (EPT) were used to obtain the AZ91 Mg alloy with bimodal microstructure. Results show that the alloy consists of coarse unrecrystallized grains of 20~60 μm and fine recrystallized grains of ~200 nm. The bimodal grains contribute to the inhomogeneous deformation under LTSRE and the acceleration effect of the static recrystallization of the deformed AZ91 magnesium alloy under EPT. In addition, the growth of the recrystallized grains is effectively restrained due to the notably low recrystallization temperature and short processing time, compared with those of the conventional static recrystallization by heat treatment. Meanwhile, abundant $Mg_{17}Al_{12}$ phases with an average size of 200 nm and regular shapes are precipitated during EPT. Consequently, the yield strength of 463 MPa and ultimate tensile strength of 527 MPa were acquired for the bimodal AZ91 alloy, which can be primarily attributed to the bimodal microstructure as well as the combined effect of fine grain strengthening, precipitation strengthening and work hardening.

Key words: AZ91 magnesium alloy; low-temperature slow rate extrusion; electric pulse treatment; bimodal microstructure; mechanical properties

Due to the high specific strength, specific modulus and other advantages, magnesium alloys have the potential to be applied in the fields of automobile, aviation and electronics, etc[1-3]. However, the comprehensive mechanical properties of magnesium alloys are still lower than those of the steel and aluminum alloys, which restricts the wider industrial application of magnesium alloys as structural materials[4,5].

Recently, bimodal microstructures have been proved as a successful route to improve simultaneously the strength and ductility of Mg alloys. In common, bimodal microstructure alloys are prepared by some special deformation techniques, such as equal channel angular pressing (ECAP)[6,7], accumulative roll bonding (ARB)[8] and hard-plate rolling (HPR)[9], and consist of the fine dynamic recrystallization (DRX) grains and the coarse unDRXed grains. The ultrafine grains provide a high strength and the coarser grains are responsible for the ductility[10-12]. Wang et al[13] reported a bimodal grain structure in AZ91 alloy by hard-plate rolling and obtained simultaneously high strength and uniform ductility of ~371 MPa and ~23%, respectively. By hot extrusion at 320 ℃, Rong et al[14] investigated the effect of bimodal-grain structure on the strength of Mg-15Gd-1Zn-0.4Zr (wt%) alloys, which exhibit ultra-high yield strength and tensile strength of 465 and 524 MPa, respectively.

Received date: March 02, 2020
Foundation item: National Natural Science Foundation of China (U1710118, U1810122, 51504162, 51601123); Outstanding Innovative Teams of Higher Learning Institutions of Shanxi (2018); Natural Science Foundation of Shanxi Province (201801D221139); Shanxi Scholarship Council of China (2016-029)
Corresponding author: Fan Jianfeng, Ph. D., Professor, Key Laboratory of Interface Science and Engineering in Advanced Materials, Ministry of Education, Taiyuan University of Technology, Taiyuan 030024, P. R. China, E-mail: fanjianfeng@tyut.edu.cn

Compared with dynamic recrystallization, it is easier for the static recrystallization to control the deformation strain, deformation temperature and recrystallization parameters, which is beneficial to acquire the expected microstructure. However, the detailed investigation on relationships between the bimodal microstructures and the static recrystallization of Mg alloys is barely reported. In our previous work, electrical pulse treatment (EPT) is helpful to accelerate the static recrystallization of the deformed Mg alloy at low temperatures for the grain refinement[15,16]. A simple and effective route to prepare bimodal grain structure for AZ91 alloy by the combined processing of low-temperature slow rate extrusion (LTSRE) and EPT was proposed in this research. During the LTSRE process, materials underwent large deformation to achieve the inhomogeneous deformed microstructure without obvious dynamic recrystallization. Then, the bimodal microstructures were obtained by static recrystallization under EPT with appropriate parameters. In addition, the microstructure and mechanical properties of the AZ91 magnesium alloys were analyzed systematically.

1 Experiment

AZ91 magnesium alloy cast sheets were cut with the diameter of 40 mm and the height of 20 mm, and then solution treated at 653 K for 2 h followed by another treatment at 688 K for 22 h (T4 treatment). After solution treatment, the samples were extruded at 523 K with the extrusion ratio of 12:1 and the extrusion rate of 0.1 mm/s. The final cross-section of the extruded product is 10 mm×10 mm. The tensile specimens with a length of 15 mm and a cross-section size of 2 mm×1 mm were machined from the extruded samples for EPT. During EPT, the pulse duration and processing time were important parameters, representing the energy of the single pulse and the energy accumulation of multiple pulses, respectively. The typical square electropulsing wave is shown in Fig.1[16]. Therefore, the effect of pulse duration and processing time of EPT on microstructures of deformed AZ91 alloy was investigated with the constant frequency and electric current of 100 Hz and 6.4×10^3 A, respectively. The temperature variation of the samples during EPT was measured at different positions (point A to point D in Fig.1) on the surfaces of samples to estimate the thermal effect of EPT. The specific EPT parameters are shown in Table 1. In this investigation, optical microscope (OM), X-ray diffraction (XRD), scanning electron microscope (SEM) and transmission electron microscope (TEM) were used to observe the microstructures of AZ91 alloys at different states. Samples for OM and SEM observation were ground and subjected to different degrees of corrosion. The observed plane was vertical to the die casting direction and parallel to the extrusion direction, and the etching agent consisted of 5 mL acetic acid, 6 g picric acid, 10 mL H_2O, and 100 mL ethanol. The volume fraction of precipitated phase and recrystallization degree were obtained through the statistical analysis by Image Pro-plus software. The tensile tests were carried out on an AG-Xplus test machine with the constant speed of 0.6 mm/min at room temperature.

2 Results and Discussion

2.1 Microstructural evolution and mechanical properties

Fig.2 shows the microstructure of AZ91 magnesium alloys before and after solution treatment. From Fig.2a, the as-cast magnesium alloy is composed of α-Mg matrix and $\alpha+\gamma$ eutectic. After T4 treatment, the grains are coarse and nonuniform with an average grain size of about 98.5 μm. Fig.3 shows the microstructure after extrusion deformation.

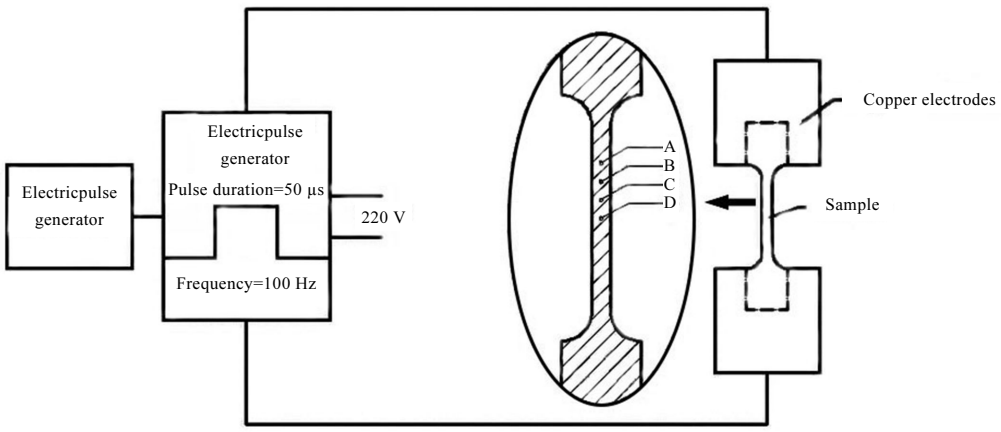

Fig.1 Schematic diagram of EPT process[16]

Table 1 EPT parameters of different samples

Sample	Duration/μs	Duty ratio	Processing time/min	Average temperature/K
EPT1	30	0.003	10	333
EPT2	40	0.004	3	373
EPT3	40	0.004	20	365
EPT4	60	0.006	3	473

The equiaxed grains transform into the deformed microstructure. The matrix grains are elongated along the extrusion direction (ED) while a small amount of deformation twins appear. Due to the coarse grains and the different grain orientations, the strains induced by extrusion are extremely inhomogeneous. A small amount of $Mg_{17}Al_{12}$ phases are precipitated at the grain boundary of deformed grains (Fig.3b). The strain and dislocation density in the deformation zones and at grain boundaries are higher than those in the undeformed zone[9].

XRD patterns of the extruded sample and EPT3 sample are shown in Fig.4. With the introduction of EPT, the peaks of the $Mg_{17}Al_{12}$ phase occur, implying that the $Mg_{17}Al_{12}$ phase are precipitated gradually during EPT. Fig.5 shows the microstructure of alloys after EPT with different parameters. Region 1 consists of coarse deformed grains and a few $Mg_{17}Al_{12}$ precipitation phases. Region 2 is composed of ultrafine recrystallized grains and abundant $Mg_{17}Al_{12}$ precipitation phases. Region 3 consists of completely recrystallized grains and moderate $Mg_{17}Al_{12}$ precipitation phases. In region 2 and 3, recrystallized grains are covered by a large number of $Mg_{17}Al_{12}$ phases and are difficult to identify. The degree of recrystallization becomes higher with the increase of pulse duration and processing time. Therefore, it can be seen from Fig.5a, 5d, and 5g that the microstructures exhibit bimodal structure including coarse unrecrystallized grains and ultrafine recrystallized grains at the same time. There are more ultrafine grains in EPT3 by comparison. The volume fractions of recrystallized grains are 49%, 55% and 71% for EPT1, EPT2 and EPT3, respectively. As the pulse duration and processing time are 60 μs and 3 min, respectively, the bimodal structure is completely displaced by the homogenous and fine recrystallized grains. Besides, the average size of the fine grains in the bimodal grain structures of EPT1, EPT2 and EPT3 is about 200 nm (Fig.6b~6d) while the average grain size of the completely recrystallized grains in EPT4 is about 900 nm (Fig.6e). The above results imply that the pulse duration of EPT accelerates the static recrystallization of the deformed microstructure more effectively than the processing time.

It is worth mentioning that a large number of $Mg_{17}Al_{12}$ phases are precipitated at grain boundaries and inside the grains and the precipitation of $Mg_{17}Al_{12}$ phases is closely related to EPT (Fig.4 and Fig.6). The amount of $Mg_{17}Al_{12}$ phases increases firstly with the increase of pulse duration and processing time (Fig.5b, 5e and 5h), and then decreases as the pulse duration continually increases to 60 μs (EPT4, Fig.5k). For EPT3, the content of the precipitated phase reaches the maximum value. The volume fraction of $Mg_{17}Al_{12}$ phase is 20%, 29%, 46% and 41% for EPT1, EPT2, EPT3 and EPT4, respectively. In addition, as shown in Fig.6, the average size of $Mg_{17}Al_{12}$ phase in EPT1 and EPT2 is about 100 nm. With the improvement of the processing time of 20 min, the average size of $Mg_{17}Al_{12}$ phase in EPT3 increases to about 200 nm. Furthermore, the average size of $Mg_{17}Al_{12}$ phase in EPT4 rises to about 300 nm when the pulse duration continually increases to 60 μs.

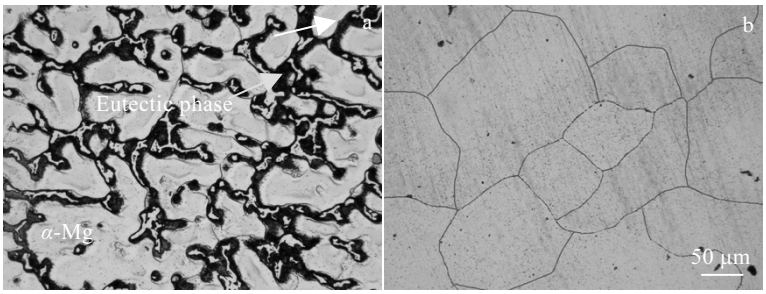

Fig.2 OM microstructures of as-cast (a) and solution treated (b) AZ91 alloy

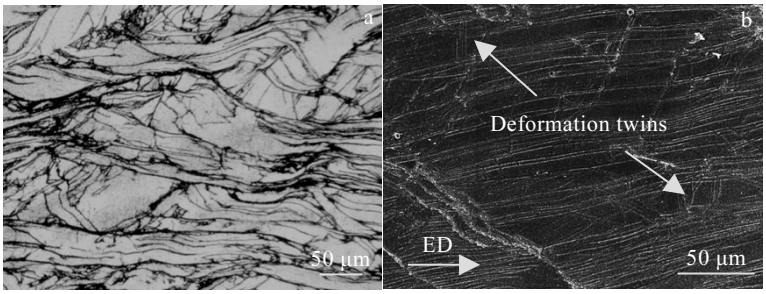

Fig.3 OM (a) and SEM (b) microstructures of extruded AZ91 alloy

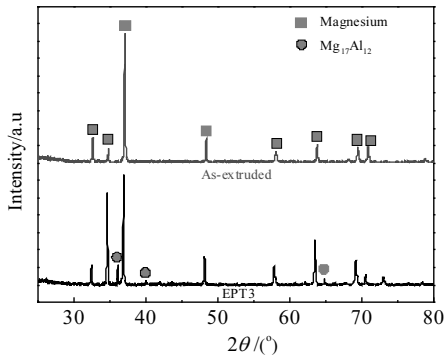

Fig.4 XRD patterns of as-extruded sample and EPT3

During the EPT, the high-speed electrons collide with the metal atoms in the magnesium alloy to enhance the amplitude of the atomic vibration. The energy of the high-speed electron propagates in the form of heat and then causes the temperature rise of the materials. The surface temperatures of samples treated under different EPT conditions were measured by a thermometer. The highest measured temperature of each sample is shown in Fig.7b. As the pulse duration increases, the more Joule heat is generated by EPT and the Joule heat is more sensitive to the pulse duration rather than the processing time.

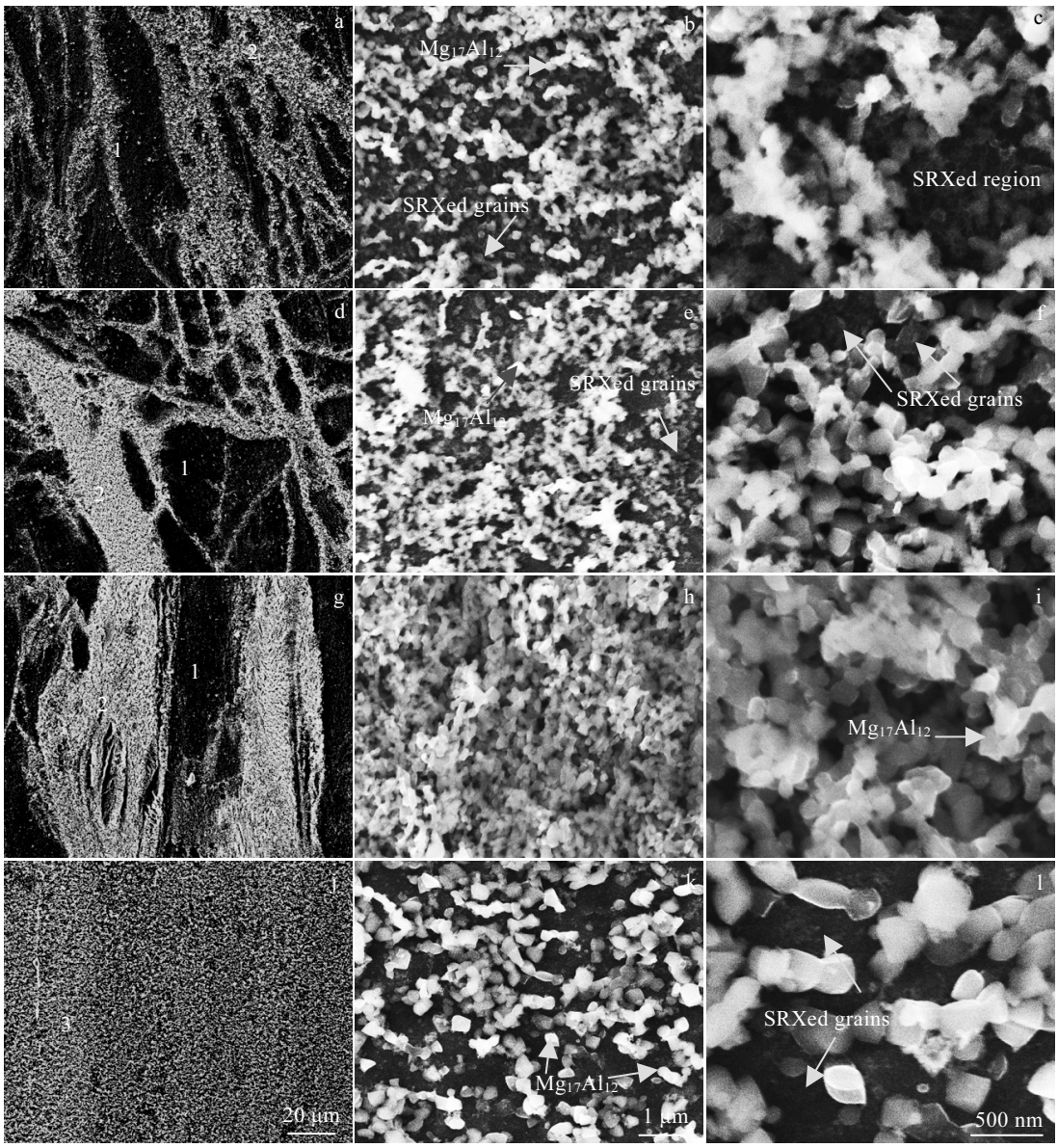

Fig.5 SEM images of samples under different EPT conditions: (a) EPT1; (b, c) high magnification of region 2 in Fig.5a; (d) EPT2; (e, f) high magnification of region 2 in Fig.5d; (g) EPT3; (h, i) high magnification of region 2 in Fig.5g; (j) EPT4; (k, l) high magnification of region 3 in Fig.5j) (region 1, 2 and 3 represent the precipitate free region, high-density precipitate region and uniform precipitate region, respectively)

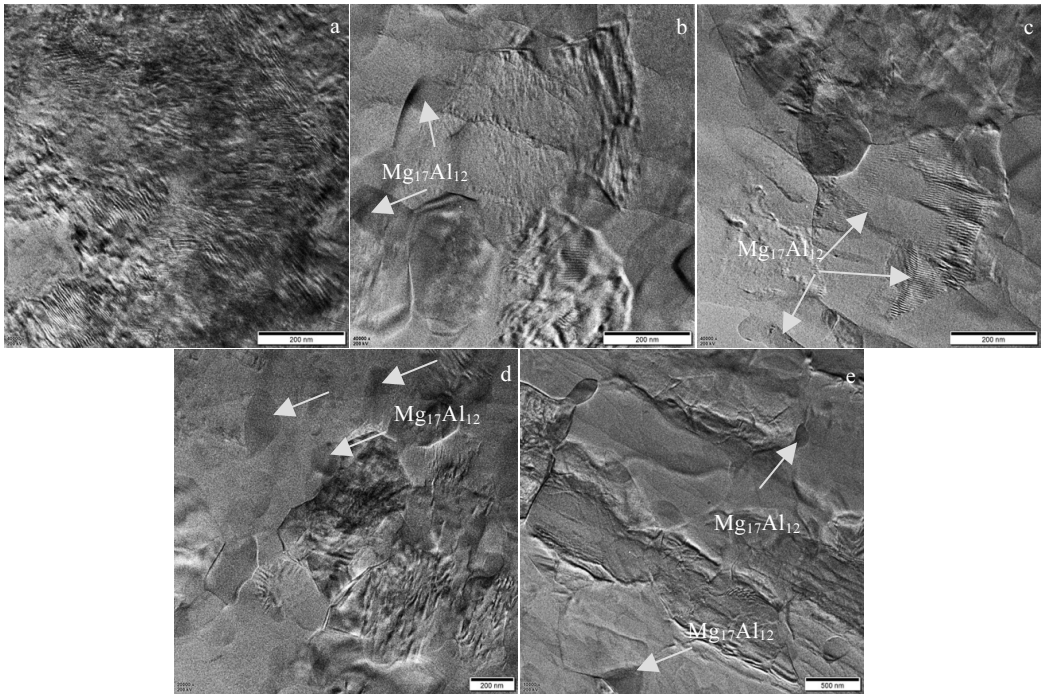

Fig.6 TEM images of extruded (a), EPT1 (b), EPT2 (c), EPT3 (d), and EPT4 (e) samples

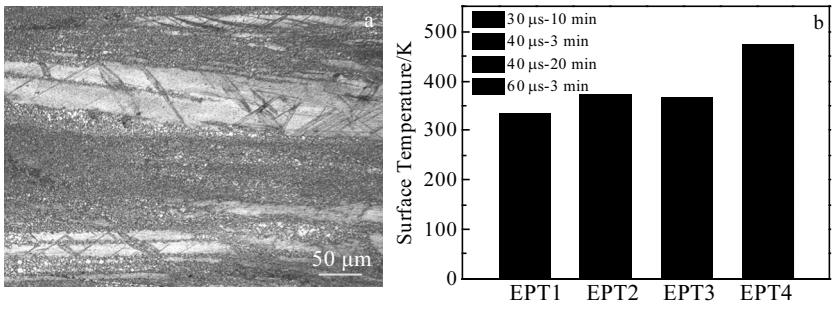

Fig.7 Microstructure of sample heated at 473 K for 60 min (a); surface temperatures of samples under different annealing conditions (b)

It can be seen from Fig.7a that the sample is not completely recrystallized even after being heated to 473 K for 60 min. The sample still maintains deformed microstructure with obvious twins and massive elongated grains. The proportion of recrystallization is less under this condition than that at the same temperature under EPT with processing time of 3 min. This phenomenon indicates that EPT is not a simple heating process. In addition to thermal effect, the athermal effect also promotes the recrystallization process.

The mechanical properties of AZ91 magnesium alloy at different states are shown in Fig.8. Due to the work hardening, the ultimate tensile strength (UTS) and 0.2% proof stress (YS) of the LTSREed sample greatly increase to 443 and 389 MPa, respectively. After EPT, the tensile properties of samples with bimodal structures improve, compared with the LTSREed sample, and EPT3 with duration of 40 μs and processing time of 20 min shows the best comprehensive properties of 463 MPa in YS, 527 MPa in UTS and 5.7% in elongation. Before the static recrystallization is completed, the improvement of YS and UTS positively related to the degree of recrystallization and the volume fraction of $Mg_{17}Al_{12}$ phase. In addition, EPT4 with completely recrystallized structure shows lower UTS (450 MPa) and YS (320 MPa), but higher elongation (10%) than those of samples with the bimodal structures and the LTSREed sample. The tensile properties in this research are prominent for the conventional AZ91 alloy. Fig.9 shows the typical fractures of as-extruded and EPTed AZ91 alloys after tensile test. The as-extruded sample tends to fail brittlely by cleavage fracture or quasi-cleavage fracture due to the deformed microstructure, as shown in Fig.9a. After EPT, the specimen EPT4 shows ductile failure, which is evidently attributed to the grain refinement. It is noted that the amount of dimples in Fig.9c is much more than that in Fig.9a, and some spherical features appear on the fracture surface which is related with the fine second phases embedded in the matrix. Fig.9b and 9d show the SEM micrograph near the fracture of

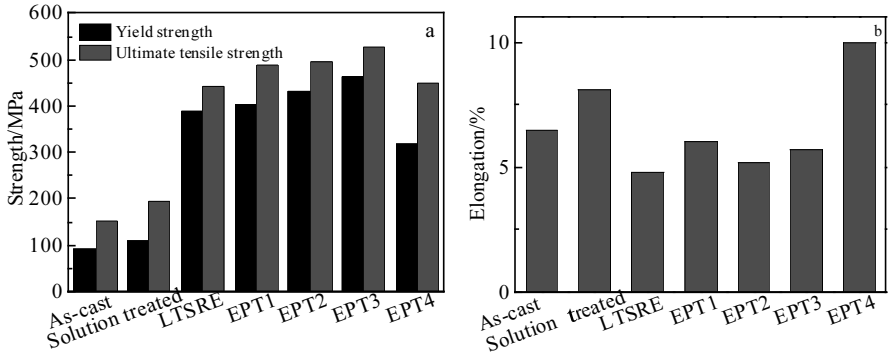

Fig.8 Strength (a) and elongation (b) of samples under different conditions

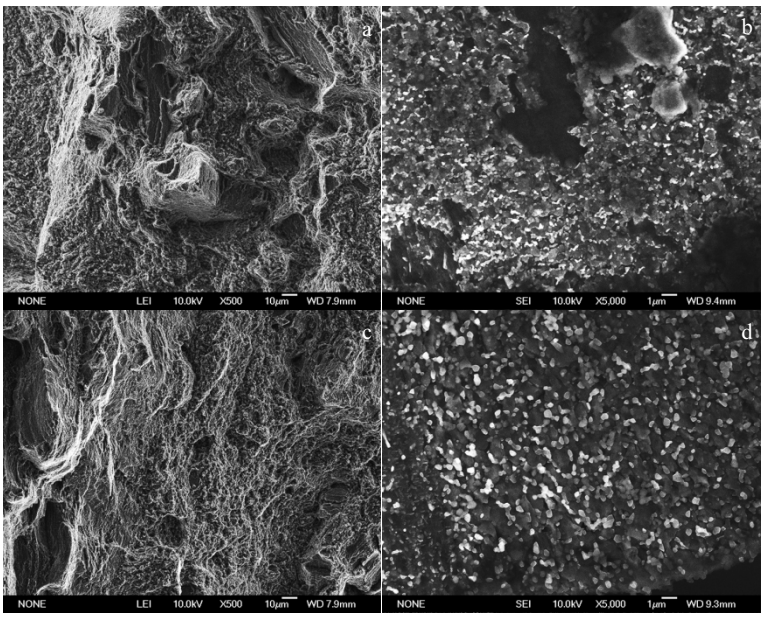

Fig.9 SEM morphologies of as-extruded AZ91 alloy (a, b) and EPT4 (c, d) near fracture location (a, c) and at fracture surface (b, d)

as-extruded sample and EPT4. It can be found that deformed region and DRX region with abundant $Mg_{17}Al_{12}$ phases near the fracture. After EPT, the microstructure transforms to complete static recrystallized grains with some spherical $Mg_{17}Al_{12}$ phases, as shown in Fig.9d.

2.2 Microstructure formation and strengthening mechanisms

The deformed microstructure is usually at non-equilibrium state due to residual stress and strain. It has a spontaneous recrystallization tendency to reduce the free energy of the system[17]. But it is difficult to transform into the equilibrium state because of the kinetic barrier at low temperature. Generally, the recrystallization of AZ91 alloy occurs at the annealing temperature of more than 573 K[18]. However, in this research, the deformed AZ91 alloy can complete recrystallization at 473 K after EPT. As a new approach to optimize microstructure, EPT can provide additional free energy to reduce the barrier of recrystallization process[19]. Besides, EPT plays a significant role to promote precipitation and spheroidizing of $Mg_{17}Al_{12}$ phase in the process. In addition, the extent and direction of the EPT effects depend on not only the EPT parameters (density of current, duration and processing time), but also the composition and prior treatment of the magnesium alloy.

Generally, EPT is always accompanied with thermal effect and athermal effect[17,20]. Therefore, the additional Gibbs free energy of EPT ΔG^{e} can be expressed as follows:

$$\Delta G^{e}=\Delta G^{e}_{th}+\Delta G^{e}_{ath} \quad (1)$$

where ΔG^{e}_{th} is the thermal effect and ΔG^{e}_{ath} is the athermal effect. In our previous study[16], the influence of the thermal effect and the athermal effect of EPT on the diffusion flux of atoms and vacancies were investigated and the result revealed that the promotional effect of the athermal effect is 14.8 times higher than that of the thermal effect. Moreover, the applying electric current accelerates the microstructure transformation of deformed metals and reduces the transi-

tion starting temperatures due to the enhancement of diffusion of solute atoms and the mobility of vacancies[19,21-23]. Additionally, growths of the recrystallized grains and the precipitated phase are effectively suppressed due to the low temperature (333~373 K) and short processing time (3~20 min), compared with the statement of alloy after conventional heat treatment. Besides, the regular and spherical shape of $Mg_{17}Al_{12}$ particles imply that EPT accelerates the spheroidizing of $Mg_{17}Al_{12}$ particles[24].

The schematic diagram of microstructure transformation process during the extrusion and EPT is shown in Fig.10. The basal slips occur more easily in grains with beneficial orientations[9]. It is speculated that grains with the favorable orientations undergo large plastic deformation during extrusion and have high stored energy. The regions with higher strain are more prone to experience static recrystallization and phase precipitation during EPT. In contrast, the grains with unfavorable orientations lack stored energy to initiate static recrystallization. When the duration is low, the additional Gibbs free energy provided by EPT is also insufficient to promote recrystallization of the low-strain regions. As a result, the bimodal structure with ultrafine recrystallized grains (consist of abundant precipitation phases) and unrecrystallized coarse grains (consist of a large number of dislocations) is obtained by LTSRE+EPT processing.

Generally, the increase in YS caused by grain refinement can be expressed by the Hall-Petch relationship[25,26]:

$$\sigma_y=\sigma_0+kd^{-1/2} \quad (2)$$

where σ_y is the YS, σ_0 is the material constant, k is the Hall-Petch slopes of 0.13 MPa·m$^{1/2}$, and d is the average grain size. In the present study, the increased YS results from grain refinement after extrusion and EPT can be calculated using follow equation.

$$\Delta\sigma_{\text{Hall-Petch}}=k(d_e^{-1/2}-d_c^{-1/2}) \quad (3)$$

where d_e and d_c are the average grain size of EPT and cast state, respectively; k is positively correlated with the Taylor coefficient, which is related to the crystal structure and the number of slip systems. Therefore, the grain refinement has a significant effect on improving the mechanical properties of magnesium alloys due to the large k value. Accordingly, the increased YS, due to grain refinement, is calculated as 135, 152, 196 and 124 MPa for EPT1, EPT2, EPT3 and EPT4, respectively.

After EPT, the average size of precipitated $Mg_{17}Al_{12}$ phase is less than 1 μm. Dislocation is pinned by the precipitation phase, and Orowan strengthening mechanism plays the important role. Therefore, the improvement in YS caused by Orowan strengthening can be expressed by the following equation[27]:

$$\Delta\sigma_{\text{Orowan}}=\beta\frac{0.4\mu_m b}{\pi\bar{\lambda}}\frac{\ln(\bar{d}/b)}{\sqrt{1-\upsilon_m}} \quad (4)$$

where $\bar{\lambda}$ is the $Mg_{17}Al_{12}$ phase spacing estimated by Eq.(5); β is the strengthening coefficient of 1.25; μ_m is the shear modulus of 16.5 GPa obtained by the equation $\mu_m=E/2(1+\upsilon_m)$; E and υ_m are the elastic modulus and Poisson's ration of matrix of 44.6 GPa and 0.35, respectively; b is the Burgers vector of 0.32 nm.

$$\bar{\lambda}=\bar{d}\left(\sqrt{\pi/4f}-1\right) \quad (5)$$

where $\bar{d}$ is the average diameter of $Mg_{17}Al_{12}$ phase, f is the volume fraction of $Mg_{17}Al_{12}$ phase. Combining Eq.(4) and Eq.(5), it can be concluded that $\Delta\sigma_{\text{Orowan}}$ increases with the increase of f and decrease of $\bar{d}$. The increment of YS owing to Orowan strengthening is 60, 92.4, 111 and 62 MPa for EPT1, EPT2, EPT3 and EPT4, respectively.

Because of the work hardening of polycrystals, the magnitude of the flow stress is closely related to the dislocation density inside the grains. The dislocations are hindered during the slipping process, which increases the dislocation density and causes the stress concentration. Therefore, the increase in the YS can be calculated by formula[28] as follows:

$$\Delta\sigma=M\alpha\mu b\sqrt{\Delta\rho} \quad (6)$$

where M is the average Taylor factor, with M=3 for the polycrystalline magnesium alloy; α is the material constant of 0.2; μ is the shear modulus; b is the Berners vector; $\Delta\rho$ is the difference between the dislocation densities before and after deformation calculated by Williamson-Hall method[29]. The improvement of YS due to work hardening is 51.5, 45.4 and 29.3 MPa for EPT1, EPT2 and EPT3, respectively.

Fig.11 displays the contributions of grain refinement, Orowan strengthening and work hardening on improving

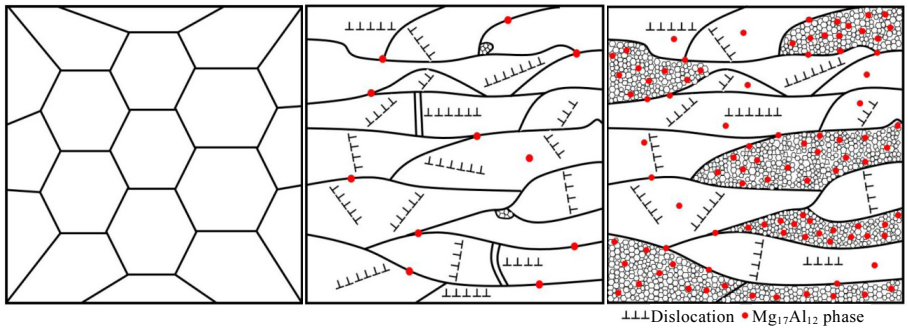

Fig.10 Schematic diagrams of microstructure transformation during extrusion and EPT

YS of EPTed alloys under different conditions. From Fig.11a, it can be concluded that the grain refinement effect shows the greatest contribution to the improvement of EPTed samples' properties. Before the static recrystallization is completed, the grain refinement effect and Orowan strengthening effect increase with the increase of recrystallization degree and $Mg_{17}Al_{12}$ phase volume fraction, respectively. However, the contribution of work hardening decreases with the increase of duration and processing time. Fig.11b demonstrates that the theoretic value of $\Delta\sigma$ is close to the experimental value. Fig.12 shows the excellent mechanical properties in this study, compared with those of samples processed by other methods.

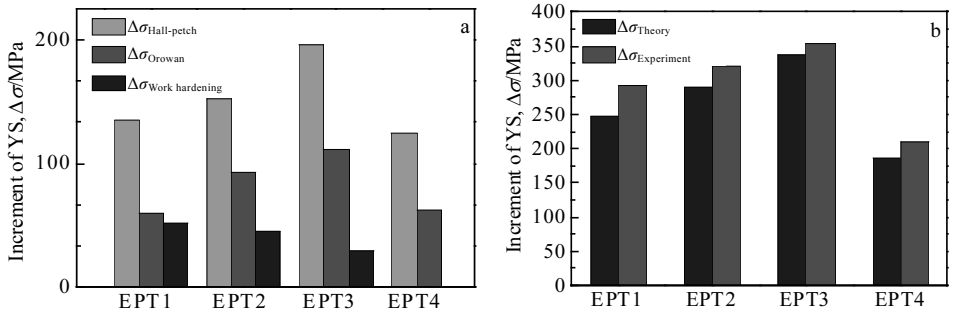

Fig.11 Theoretic increment of the yield strength (YS) based on different effects (a); comparison of theoretic and experimental YS of different samples (b)

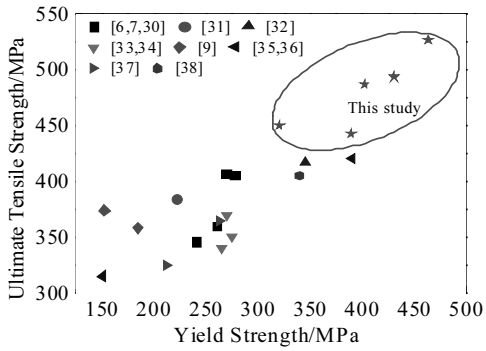

Fig.12 Comparison of mechanical properties of samples in this study and samples processed by other methods

3 Conclusions

1) The bimodal microstructure with ultrafine recrystallized grains of about 200 nm and coarse deformed grains of 20~60 μm were obtained by low-temperature slow rate extrusion (LTSRE) and electrical pulse treatment (EPT). In addition, a large amount of $Mg_{17}Al_{12}$ phases of about 200 nm are precipitated during EPT process.

2) The tensile properties with YS of 463 MPa, UTS of 527 MPa and elongation of 5.7% are acquired for the processed AZ91 alloy. The improved mechanical properties are attributed to not only the grain refinement and work hardening due to the typical bimodal grain structure, but also the Orowan strengthening effect resulting from the abundant spherical $Mg_{17}Al_{12}$ precipitated particles.

3) EPT can accelerate the static recrystallization and phase precipitation of deformed AZ91 magnesium alloy and decrease the microstructure transformation starting temperature. Additionally, the growths of the recrystallized grains and the precipitated phases were effectively suppressed due to the low temperature and short processing time, compared with the properties of samples processed by conventional heat treatment.

Reference

1 Suh B C, Shim M S, Shin K S *et al*. *Scripta Materialia*[J], 2014, 84-85: 1
2 Agnew S R, Nie J F. *Scripta Materialia*[J], 2010, 63: 671
3 Aghion E, Bronfin B. *Materials Science Forum*[J], 2000, 350-351: 19
4 Polmear I J. *Materials Science and Technology*[J], 1994, 10: 1
5 Luo A A. *Journal of Magnesium and Alloys*[J], 2013(1) : 2
6 Yang Z Q, Ma A B, Liu H *et al*. *Metals*[J], 2018, 8(10): 763
7 Sun J P, Yang Z Q, Han J *et al*. *Materials Science and Engineering A*[J], 2018, 734: 485
8 Pérez-Prado M T, Valle del J A, Ruano O A. *Scripta Materialia*[J], 2004, 51: 1093
9 Zha M, Zhang X H, Zhang H *et al*. *Journal of Alloys and Compounds*[J], 2018, 765: 1228
10 David W, Lee Z, Rodriguez R *et al. Scripta Materialia*[J], 2003, 49: 297
11 Wang Y M, Ma E. *Acta Materialia*[J], 2004, 52: 1699
12 Wang Y M, Chen M W, Zhou F H *et al. Nature*[J], 2002, 419: 912
13 Wang H Y, Yu Z P, Zhang L *et al. Scientific Reports*[J], 2015, 5: 17100
14 Rong W, Zhang Y, Wu Y J *et al. Materials Science and Engineering A*[J], 2019, 740-741: 262
15 Liu Y, Fan J F, Zhang H *et al. Journal of Alloys and Compounds*[J], 2015, 622: 229

16 Zhao G W, Fan J F, Zhang H *et al. Materials Science and Engineering A*[J], 2018, 731: 54
17 Du X N, Yin S M, Liu S C *et al. Journal of Materials Research*[J], 2008, 23: 1570
18 Xu X Y, Wang Y F, Wang H Y *et al. Journal of Alloys and Compounds*[J], 2019, 787: 1104
19 Qin R S, Samuel E I, Bhowmik A. *Journal of Materials Science*[J], 2011, 46: 2838
20 Zhou Y Z, Zhang W, Wang B Q *et al. Journal of Materials Research*[J], 2002, 17: 2105
21 Jiang Y B, Tang G Y, Shek C H *et al. Journal of Alloys and Compounds*[J], 2011, 509: 4308
22 Wang Z Q, Zhong Y B, Lei Z S *et al. Journal of Alloys and Compounds*[J], 2009, 471: 172
23 Jin W, Fan J F, Zhang H *et al. Journal of Alloys and Compounds*[J], 2015, 646: 1
24 Jiang Y B, Tang G Y, Shek C H *et al. Acta Materialia*[J], 2009, 57: 4797
25 Du Y Z, Qiao X G, Zheng M Y *et al. Materials Science and Engineering A*[J], 2015, 620: 164
26 Hofstetter J, Rüedi S, Baumgartner I *et al. Acta Materialia*[J], 2015, 98: 423
27 Deng K K, Shi J Y, Wang C J *et al. Composites: Part A*[J], 2012, 43: 1280
28 Gutiérrez I, Altuna M A. *Acta Materialia*[J], 2008, 56: 4682
29 Ma K, Wen H, Hu T *et al. Acta Materialia*[J], 2014, 62: 141
30 Yuan Y C, Ma A B, Jiang J H *et al. Journal of Alloys and Compounds*[J], 2014, 594: 182
31 Chen L, Li S S, Chu X R *et al. Materials Letters*[J], 2019, 241: 104
32 Lee T, Yamasaki M, Kawamura Y *et al. Metals and Materials International*[J], 2019, 25: 372
33 Jiang Y B, Guan L, Tang G Y *et al. Journal of Alloys and Compounds*[J], 2015, 626: 297
34 Jiang Y B, Tang G Y, Shek C H *et al. Journal of Materials Research*[J], 2009, 24: 1810
35 Okayasu M, Muranaga T. *Journal of Materials Engineering and Performance*[J], 2017, 26: 4977
36 Nie K B, Wang X J, Deng K K *et al. Journal of Alloys and Compounds*[J], 2014, 617: 979
37 Kim S H, Lee J U, Kim Y J *et al. Materials Science and Engineering A*[J], 2017, 703: 1
38 Pérez-Prado M T, Valle del J A, Ruano O A. *Materials Letters*[J], 2005, 59: 3299

低温慢速挤压和电脉冲处理制备具有优异力学性能的 AZ91 双峰合金

武红飞[1]，樊建锋[1,2]，单召辉[1]，张 华[1,2]，张 强[1,2]，邓坤坤[1,2]，吴玉程[1]，李卫国[1]，董洪标[3]，许并社[1]
(1. 太原理工大学 新材料界面科学与工程教育部重点实验室，山西 太原 030024)
(2. 山西省先进镁基材料重点实验室，山西 太原 030024)
(3. 莱斯特大学 工程系，英国 莱斯特 LE1 7RH)

摘 要：通过低温慢速挤压(LTSRE)和电脉冲处理(EPT)获得具有双峰结构的 AZ91 镁合金，这种结构由粗大的尺寸为 20~60 μm 的未再结晶晶粒和细小的尺寸约为 200 nm 的再结晶晶粒组成。双峰晶粒结构的形成原因主要是 LTSRE 过程中的不均匀变形以及 EPT 对于变形 AZ91 镁合金静态再结晶的加速效应。与常规热处理时的静态再结晶过程相比，EPT 过程的再结晶温度显著降低，处理时间明显缩短，有效抑制了再结晶晶粒的生长。同时在 EPT 过程中析出了大量形状规则的 $Mg_{17}Al_{12}$ 相，平均尺寸约为 200 nm。因此，本研究获得了屈服强度为 463 MPa 和抗拉强度为 527 MPa 的 AZ91 双峰合金，这主要归功于双峰组织以及细晶强化、析出强化和加工硬化的共同作用。

关键词：AZ91镁合金；低温慢速挤压；电脉冲处理；双峰组织；力学性能

作者简介：武红飞，男，1995 年生，硕士生，太原理工大学新材料界面科学与工程教育部重点实验室，山西 太原 030024，E-mail: 844868310@qq.com